

CHAPTER 6

FAULT KINEMATICS

Brittle deformation is frequently quantified using fault kinematic analysis methods. These methods are based on measurements of mesoscale faults and associated striae (“fault-striae data”). Fault kinematic analysis commonly determines the reduced stress tensor, i.e. the directions of principal stresses ($\sigma_1 > \sigma_2 > \sigma_3$), and the stress ratio $R = (\sigma_2 - \sigma_3) / (\sigma_1 - \sigma_3)$ at a certain locality¹. Fault kinematic analysis therefore yield information of the orientation and shape of the stress ellipsoid but does not yield information about the absolute values of stress.

There are three basic assumptions of fault kinematic analysis which have to be verified if fault kinematic data are interpreted in terms of stress:

- (1) The stress tensor is symmetric, i.e. deformation is coaxial, pure shear
- (2) deformation is homogeneous
- (3) faulting is consistent with the Mohr-Coulomb yield criterion (Coulomb, 1773), i.e. faults develop parallel to σ_2 and with an material-inherent fracture angle (the “angle of internal friction”) to σ_1

When interpreting fault kinematic data, it should always kept in mind that mostly none of these assumptions is realized in nature!

Pure shear and homogeneous deformation (assumptions 1 and 2) may be a realistic simplification at a small (outcrop) scale but probably not at regional scale (e.g. Pollard et al., 1993, Homberg et al., 1996, Jiang and Williams, 1999, Tikoff and Wojtal, 1999, Gapais et al., 2000). Consequently, inferred stress tensors reflect a local state of stress.

¹ Although the usage of the term “stress” has become established in fault kinematic analysis, it should be kept in mind that the analysis actually deals with strain. The calculated axes should therefore be called “kinematic axes” rather than “principal stress axes”. In the literature, confusion has arisen from the undefined and mixed use of terms related to stress (tension, compression) and strain (extension, contraction) in the interpretation of fault kinematic data (see discussion in Marrett and Peacock, 1999). In this work, stress-related terms (stress tensor, principal stresses, and stress ratio) are used when dealing with the results of fault kinematic analysis to facilitate correlation with other publications. When interpreting the results, however, strain-related terms are preferred to account for the principal nature of the data set.

Assumption 3 is strictly only valid in isotropic rocks, where faults may develop parallel to σ_2 at an fracture angle varying between 0° (pure tensional fractures) to 30° (shear fracture) to σ_1 (Griffith, 1921, Coulomb, 1773). Experimentally obtained fracture angles range between 0° and 40° and are mostly around 30° , which might therefore be a reasonable approximation in most natural cases (e.g. Handin et al., 1963, Byerlee, 1978). However, in anisotropic rocks, pre-existent discontinuities (for example, existing fractures, foliations, bedding planes) may be reactivated irrespective of their orientation with respect to σ_1 . If the applied differential stress is low and if the pore fluid pressures are sufficiently high to exceed lithostatic pressures, even angles of $45 - 90^\circ$ are observed (e.g. Secor, 1965, Sibson, 1985).

From the above follows that fault kinematic data actually should not be interpreted as stress-related. Instead, an interpretation of the derived tensors as reflecting the local finite strain (P, B, T) is proposed. In this work, stress-related terms (stress tensor, principal stresses, stress ratio) are used consequently when dealing with the results of fault kinematic analysis to facilitate correlation with other publications. Interpretation will follow, however, purely kinematic ideas.

6.1 Fault kinematic analysis

6.1.1 Data acquisition

During field work, more than 1100 mesoscale (cm – meter scale) faults and associated striae have been measured in more than 100 localities. In each locality, as many as possible fault-striae data have been acquired. Generally, a number of 20 to 40 fault-striae data per site are sufficient to yield a statistically stable tensor solution (Arlegui-Crespo and Simon-Gomez, 1998). The data set covers all directions with a dominance of N-S to NE-SW and WNW-ESE striking, steeply dipping faults (Fig. 6.1). Kinematic indicators used to infer shear direction and shear sense on a certain fault plane comprise slickensides (fibrous crystal growth) and Riedel shears (e.g. Petit, 1987). Fibrous crystals observed on fault planes in the study area are dominantly quartz in granitoid rocks and calcite in volcano-sedimentary rocks area, occasionally chlorite and iron-oxides/-hydroxides occur. It has been impossible to conclusively show a temporal succession of slickensides from crosscutting relationships in outcrops where more than one slickenside population exists on one fault plane.

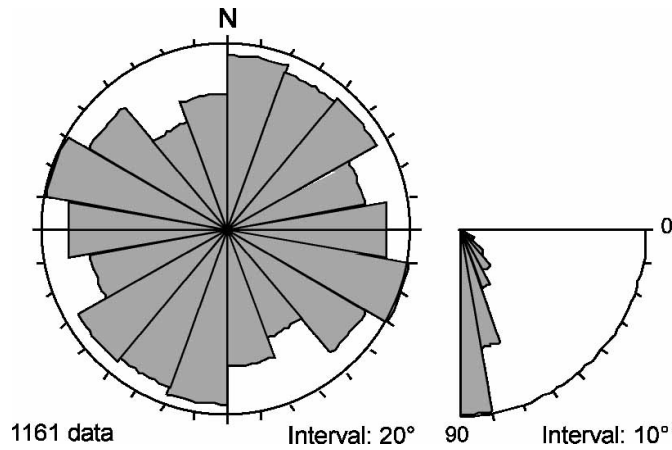


Fig. 6.1: Distribution of faults used for fault kinematic analysis.

6.1.2 Processing

For all kind of fault kinematic data visualization, processing, and analysis, the computer program *TectonicsFP* by Reiter and Acs (2000) has been used. After input of the raw data, datafiles are corrected so that all striae lie perfectly on the respective fault planes (no misfit). To do this, fault-striae are rotated along a great circle, which is defined by the striae and the pole of the fault plane, to align on the fault plane. This operation is necessary to be carried out before further processing of the data files.

Fault-striae data can be represented graphically in equal area, lower hemisphere stereonets by two different ways (Fig. 6.2): (1) The Angelier plot (Angelier, 1979) displays fault planes as great circles and an arrow pointing in the direction of relative slip of the hanging wall; (2) the Hoeppener plot (Hoeppener, 1955), also called tangent lineation plot, displays poles to faults with the arrows drawn in the pole point as tangents to the common great circle of the fault plane and the striae. The arrow points in the direction of slip of the hanging wall. This representation is particularly useful for large data sets.

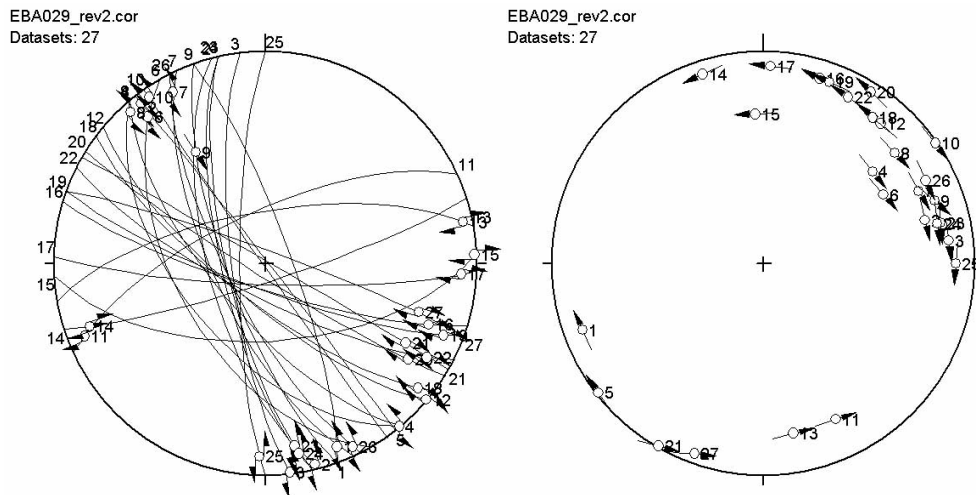


Fig. 6.2: Fault kinematic data representation: a) Angelier plot, b) Hoeppener plot.

Data sets may include several fault populations (heterogeneous data sets) consistent with distinct stress tensors. Thus, separation of fault populations has to be done before analysis. Data separation has been done after calculation of the P-T axes following Turner (1953): For every fault plane, a contraction (P-axis) and extension axis (T-axis), both lying in the plane given by the fault plane and the striae, is constructed with an angle τ between the fault plane and the P-axis. τ corresponds to the fracture angle defined above and may vary between 0° and 90° . In a first step, all data are considered and the best fit τ angle² is used to construct the P-T axes. Data separation is then done in an equal area, lower hemisphere stereoplot of the P-T axes. If several fault populations belonging to distinct stress tensors exist in the data set, several clusters appear on the plot and data can be separated accordingly. In the same way, single data which cannot be related to a population are erased from the data set.

6.1.3 Data analysis

Two common numerical methods of fault kinematic analysis are used in this work: Numeric dynamic analysis, NDA (after Spang, 1972) and direct inversion, INVERS (after Angelier and Goguel, 1979).

NDA has a similar methodical approach as the P-T method of Turner (1953). Assuming coincidence of σ_1 with P and σ_3 with T (i.e. irrotational deformation), NDA calculates a stress tensor for each fault-striae set. Summation of the stress tensors of all fault-striae sets at a locality and division by the number of sets yields the bulk stress tensor. The

² The best fit τ angle is the angle at which clustering of P- and T-axes of the data set is maximal. The “Regelungsgrad” R of Wallbrecher (1986) has been used as a measure of clustering.

orientations and relative values of the principal stresses are derived from the eigenvalues and eigenvectors of the bulk stress tensor.

INVERS is based on a least square minimization of the angles between the calculated directions of maximum shear stress acting along the fault planes and the measured striae which lead to the determination of the reduced stress tensor defined by the orientation of the principal stress axes and the stress ratio. The orientations and relative values of the principal stresses are derived from the eigenvalues and eigenvectors of the bulk stress tensor.

Sperner (1996) discussed the advantages and disadvantages of NDA versus INVERS. She concluded that INVERS fails if less than three independent fault planes are present in the data set, for example if the data set comprises two conjugate fault sets. This is because the regression used by INVERS to estimate the best-fit tensor is only statistically optimal if data are distributed. Actually, from the mathematical point of view, a tensor solution based on less than four independent fault planes is meaningless because the solution space is not completely determined (Oncken, pers. comm.). In the case of triaxial deformation, NDA has limitations because both P- and T-axes show a diffuse orientation, prevailing fixing of kinematic axes. INVERS handles those data sets without problems.

The results of fault kinematic analysis are represented in so-called “beachball”-plots, where compressive and distensive dihedras are shown together with the principal stress axes in an equal-area, lower hemisphere stereoplot (Fig. 6.3). To avoid mixing up with seismic focal mechanisms which are commonly also displayed by beachballs (black = distensive, white = compressive), results from fault kinematic analysis are represented by white (distensive) and grey (compressive) dihedras.

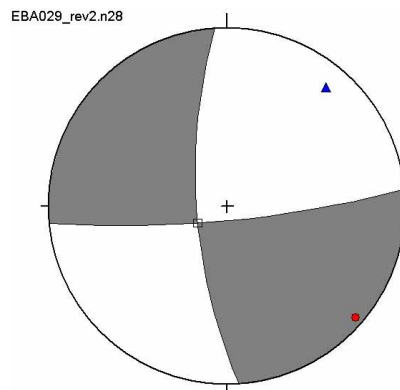


Fig. 6.3: Representation of fault kinematic analysis results with a “beachball”-plot (distensive dihedra = white, compressive dihedra = grey). Principal stress directions indicated by dot (σ_1), open square (σ_2), and triangle (σ_3).

Using the bulk stress tensor, both methods calculate the angles β between the calculated directions of maximum shear stress acting along the particular fault planes and the measured striae (Sperner, 1996). The variation of β is visualized in a fluctuation diagram (Fig. 6.4 a). The fluctuation F gives the arithmetic mean β angles which can be used as a measure of the quality of the tensor solution: The lower F , the better the solution. If fault-striae data with $\beta > 30^\circ$ are inherent the data set, they may be part of another fault population. A dimensionless Mohr circle (Mohr, 1900, 1904) in the σ_1 - σ_3 plane visualizes the normal (σ_n , abscissa) and shear stress (τ , ordinate) introduced by the stress vector for each fault plane (Fig. 6.4 b). The shear conditions for each fault plane are calculated after a graphical solution of Wallace (1951). The position between σ_1 and σ_3 , where the two circles meet, is defined by the stress ratio $R = (\sigma_2 - \sigma_3 / \sigma_1 - \sigma_3)$. Normalization is achieved by fulfilling $\sigma_1 + \sigma_2 + \sigma_3 = 0$.

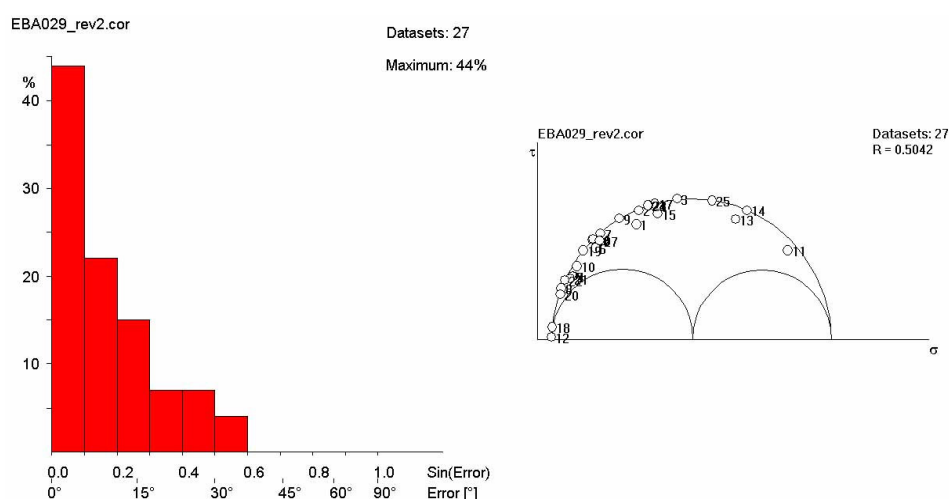


Fig. 6.4: Representation of data output: a) Fluctuation plot, b) Mohr diagram.

6.2 Results of fault kinematic analysis

In this work, 59 local stress tensors have been derived based on 821 fault-striae data from 52 localities. The resultant stress tensors are summarized in Table 6.1 and displayed as beachballs and stereoplots in Figs. 6.5 and 6.6, respectively. 56 of these tensors have been derived from the usage of NDA, only three necessitated INVERS due to triaxial deformation. τ angles used for NDA are chosen for each data set individually, generally the best-fit angle with the highest *Regelungsgrad* has been used. The mean τ angle for the whole data set is 42° . Tensor solutions for sites with granitoid and volcanic rocks (lavas) have a tendency toward slightly higher and less variable τ angles compared to those with volcano-sedimentary rocks. This is probably because they are more competent and isotropic than volcano-sedimentary rocks, which show abundant pre-existent discontinuities (e.g. bedding planes).

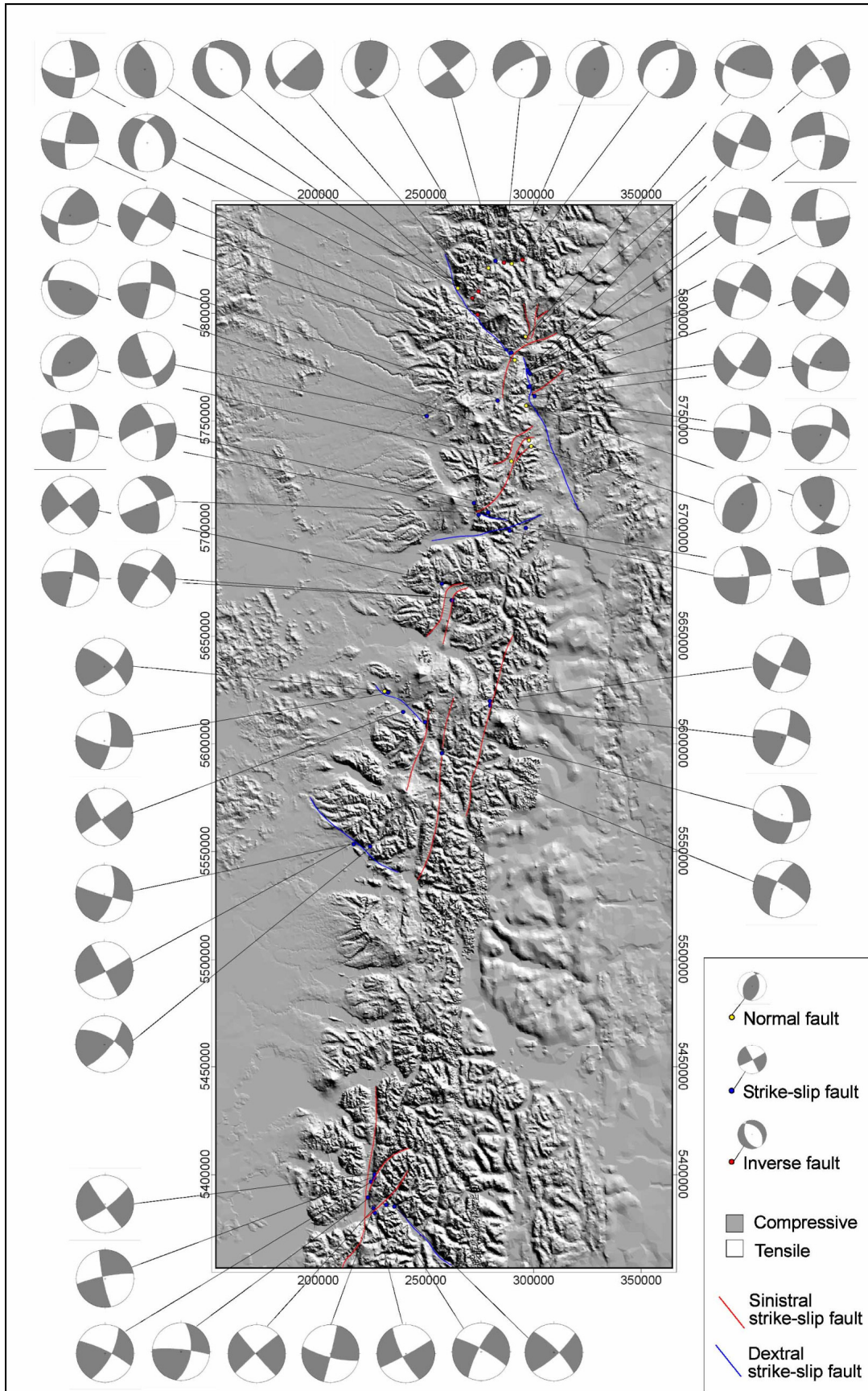


Fig. 6.5: Results of fault kinematic analysis represented by beachballs. Dots indicate the locality of analysis. Yellow dots are normal fault solutions, blue dots strike-slip, red dots inverse (UTM19S projection). The traces of known or newly mapped strike-slip faults for which fault kinematic analysis verified the kinematics are indicated by blue (sinistral) and red (dextral) lines.

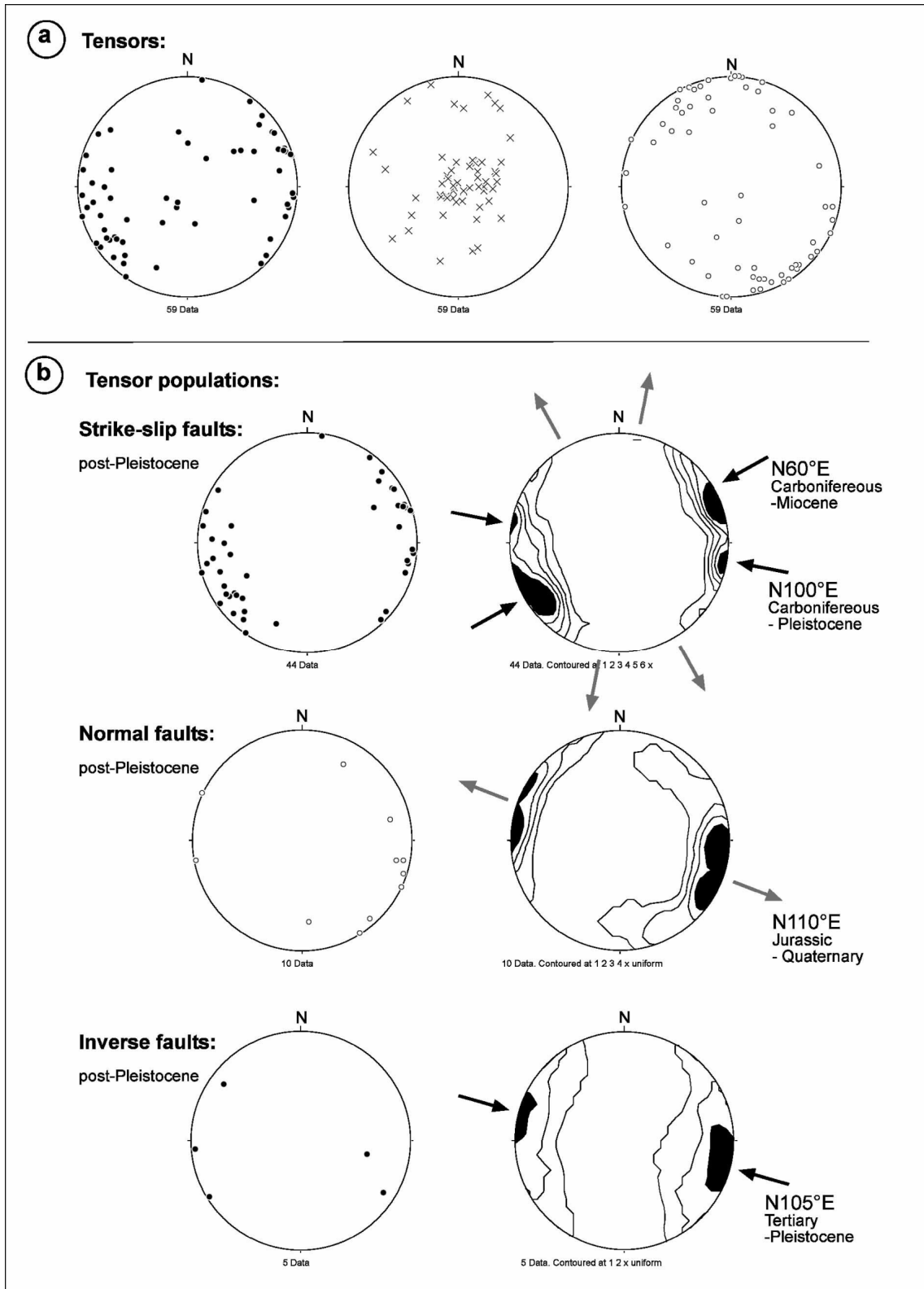


Fig. 6.6: Results of fault kinematic analysis represented by stereoplots: a) all tensors (left = P-axes, middle = B-axes, right = T-axes), b) tensor populations.

The mean fluctuation F for this data set is $12^\circ (\pm 5^\circ, 1\sigma \text{ standard deviation})$ indicating a high confidence of the bulk tensor solutions. The Quality of each stress tensor has been quantified by introducing a factor $Q = N$ (number of measured faults)/ F (fluctuation)

and by defining the following three classes: $Q < 0.67$ (poor), $Q = 0.67-1.33$ (good), $Q > 1.33$ (excellent). The number of measured faults used for the tensor calculation range from 5 to 45. 22 tensors have an excellent quality, 24 are of good quality. 13 tensors are of poor quality and have to be treated with caution during interpretation. Stress ratios average at $R = 0.5 (\pm 0.1, 1\sigma \text{ standard deviation})$, which reflects the dominantly plane strain character of deformation in the study area.

Based on the orientation of the principal stress axes, tensors are grouped into strike-slip faults (B-axes plunge $> 45^\circ$), normal faults (P-axes $> 45^\circ$), and inverse faults (T-axes plunge $> 45^\circ$, Fig. 6). The majority of tensors (44) indicate strike-slip deformation, 10 show normal faulting, and 5 inverse movements (Fig. 6.6 b). Kinematic axes of the tensor solutions suggest a heterogeneous deformation pattern. Strike-slip solutions show a bimodal distribution indicating contraction in NE-SW ($N60^\circ E$) and WNW-ESE ($N100^\circ E$) directions and corresponding NW-SE and NNE-SSW directed extension. Normal fault solutions vary from extension in N-S direction to extension in E-W direction. Inverse fault solutions indicate WNW-ESE contraction. All these tensor populations occur in rocks younger than Miocene.

6.3 Discussion

6.3.1 Temporal versus spatial heterogeneity of deformation

Fault kinematic analysis suggests the existence of at least four different tensor populations each of which can be related to a distinct kinematic regime (Fig. 6.6): (1) A strike-slip regimes with NE-SW ($N60^\circ E$) oriented shortening directions, (2) another strike-slip regime with E-W ($N100^\circ E$) oriented shortening directions, (2) WNW-ESE extension associated with thinning (normal faulting), and (3) WNW-ESE shortening associated with thickening (inverse faulting).

The observation of different kinematic regimes in general may be related either to temporal or to spatial heterogeneous deformation. More specifically, different kinematic regimes may reflect on or more of the following scenarios: (1) temporally successive tectonic phases, (2) kinematic partitioning of deformation, or (3) short term temporal fluctuations and reversals of the stress field (“bounce” structures, Means, 1999), for example during the seismic cycle (stick-slip).

In the first case, tectonic phases, tensor populations are expected to correlate with the age of the rock in which they are represented. For instance, the youngest rocks should

show only one tensor population whereas older rocks may preserve evidence for additional, older tensor populations. Accordingly, several successive kinematic regimes (“paleostress regimes”) may be deduced from the bulk of observed tensors.

In the second case, kinematic partitioning, tensor populations should correlate with structures (e.g. faults) observed nearby the outcrop from which the tensor has been derived. If those structures are kinematically compatible, that means, if they are active coevally during the same tectonic phase, different tensor populations mirror local deformation which may deviate significantly from bulk regional deformation. Kinematic partitioning is a natural process and occurs at almost all scales of observation (plate boundaries, fault zone systems, fracture sets, fault breccias, grain boundaries) and results mostly in a spatially heterogeneous deformation pattern.

In the third case, temporal fluctuations, there is neither a correlation with age of the sampling site nor with its location along master faults. Instead distinct tensor populations may exist at the same place at the same time, in geologic time scales (> 10 ka – 1 Ma). They rather represent a non-stationary, reversed, or transitional stress field during the seismic cycle. Typically, those transient stress fields show a permutation of spatially coherent kinematic axes.

Age correlations

In the current data base, no clear correlation between tensor correlations and age has been observed. Instead, all tensor population seem to be Pliocene or younger: Strike-slip tensors occur in rocks varying in age from Carboniferous (Panguipulli batholith) to Quaternary (active volcanic arc) with the youngest sites being two Pliocene-Quaternary sites giving one poor (PAN139, $Q = 0.28$) and one excellent (PAN029, $Q = 2.00$) tensor solutions. Normal fault tensors occur in rocks with Jurassic (Northern Patagonian Batholith, NPB) to Quaternary (active volcanic arc) ages with the youngest sites being two Pliocene-Quaternary sites giving one poor (EBA042, $Q = 0.48$) and one good (PAN066, $Q = 0.72$) tensor solution. Inverse fault tensors are derived from Miocene (NPB, Fm. Cura-Mallín) to Pliocene-Pleistocene (Fm. Malleco) rocks with the youngest site giving an excellent tensor solution (PAN082, $Q = 1.76$). Therefore, all kinematic regimes are interpreted as coeval at a geologic timescale. EBA029 and EBA030 both show two strike-slip tensors which are parallel but of opposite senses. They may reflect the existence of reversals in the stress field.

Spatial relationships with master faults

The correlation of individual local strain tensors with major fault zones becomes evident from Fig. 6.5. Sites located along NNE-SSW trending fault zones display dominantly strike-slip tensor solutions with a NE-SW directed shortening direction consistent with a dextral sense of shear. Where those arc-parallel dextral faults trend more to the east, i.e. have Riedel shear geometry with respect to the main faults, or form eastward bending splays or horsetail structures, shortening directions successively rotate clockwise to an E-W direction. Normal faulting is associated with eastward bending structures in the northern part of the study area (e.g. Lonquimay area). Sites located along E-W to NW-SE trending fault zones show strike-slip tensors with, respectively, NE-SW to WNW-ESE directed shortening consistent with sinistral strike-slip. This spatial relationship of local strain tensors with fault zones indicate that the heterogeneous entirety of local strain tensors is an effect of kinematic partitioning of deformation.

Fig. 6.7 visualizes how the bimodal distribution of strike-slip fault kinematic data (Fig. 6.7 a), which make up the majority of data, is biased by the SC-like kinematics of major faults within the LOFZ system: If deformation would be homogeneous, local strain tensors should be uniform and parallel to the regional finite strain tensor, which reflects the bulk deformation (Fig. 6.7 b left). In the case of kinematic partitioning of bulk deformation into two kinematically linked fault sets, the resulting local strain tensors deviate significantly from the hypothetical regional finite strain tensor. In the Southern Andean intra-arc zone, NE-SW ($N60^{\circ}E$) directed shortening is associated with arc-parallel dextral strike-slip faults. E-W ($N100^{\circ}E$) directed shortening is associated with arc-oblique sinistral strike-slip faults.

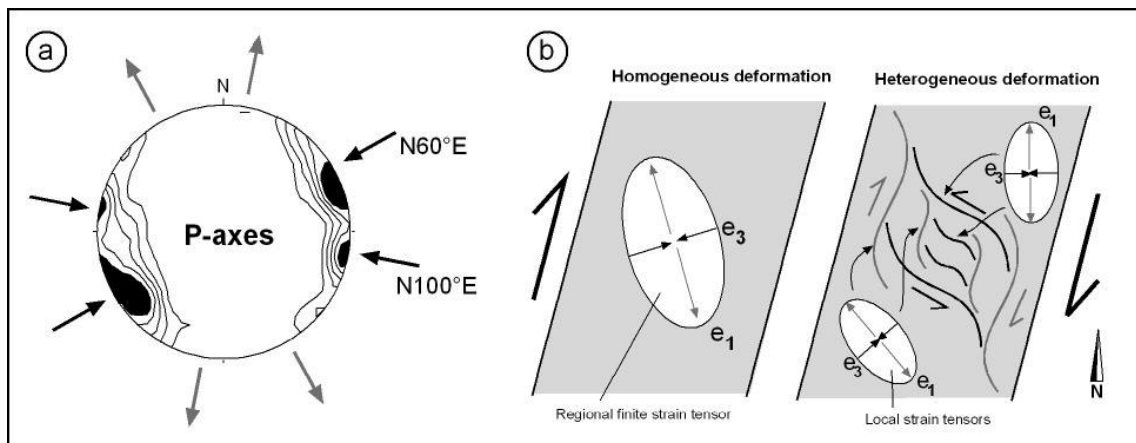


Fig. 6.7: Bimodal distribution of fault kinematic data due to strain partitioning into a kinematically linked fault system: (a) P-axes from fault kinematic analysis, (b) sketch illustrating the effect of strain partitioning.

6.3.2 Along-arc variation of the deformation field

The study area forms the link between transtensional tectonics related to a crustal scale horsetail structure in the north (37 - 38°S, Potent and Reuther, 2001, Potent 1003) and transpressional tectonics related to a crustal scale strike-slip duplex in the south (44 - 47°S, Cembrano and Hervé, 1993, Cembrano et al., 2002). Although dominated by strike-slip tectonics, kinematic data between 38 and 42°S show a marked spatial variability of the deformation field due to strain partitioning into the SC-like LOFZ as discussed above. This section investigates modifications of the regional characteristic (bimodal) kinematic data distribution related to different tectonic regimes in the north and to the south of the study area.

Fig. 6.8 displays the variation of kinematic data along strike of the study area (N-S). The plunges of kinematic axes along strike of the arc (Fig. 6.8 a) indicate the distribution of local tectonic regimes (strike-slip, normal faulting, thrusting/inverse faulting): Moderately to steeply dipping B-axes and subhorizontal P- and T-axes dominate between 42° (UTM 5400000N) and ca. 39°S (UTM 5750000N) indicate that this segment of the LOFZ is characterized by strike-slip faulting. In the northern part, however, kinematic axes show a pronounced variability in their orientation with subhorizontal to subvertical P-, T-, and B-axes suggesting the coexistence of thrusting (subvertical T-axes), normal faulting (subvertical P-axes), and strike-slip (subvertical B-axes) deformation.

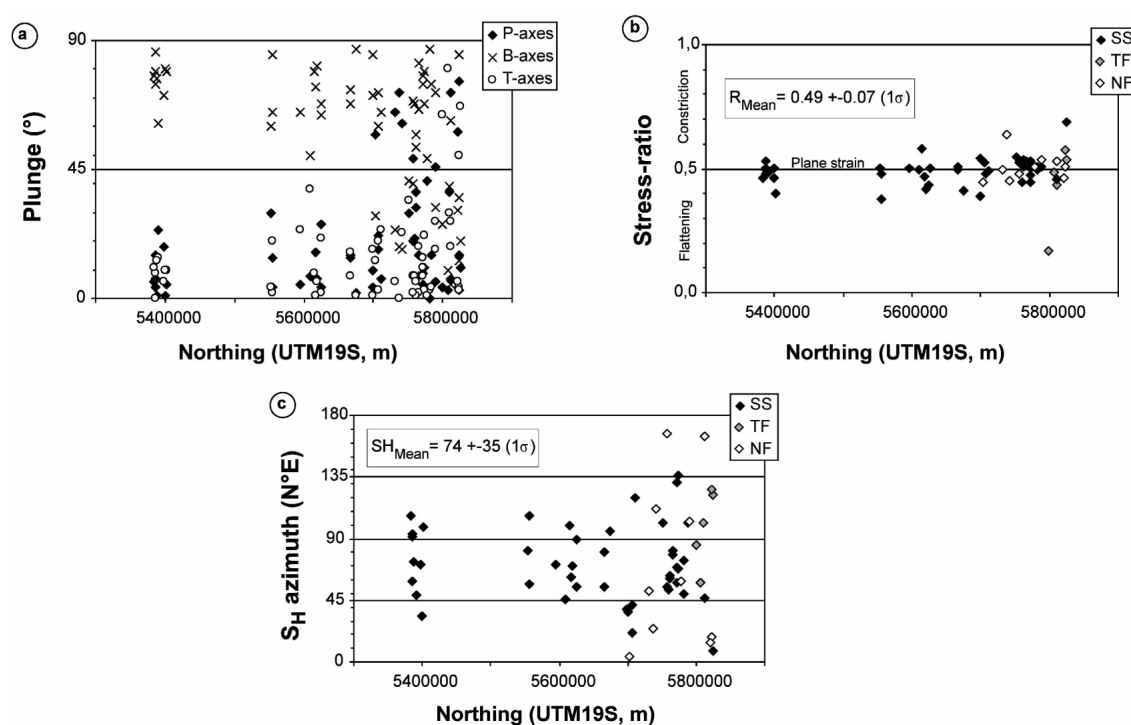


Fig. 6.8: Along-arc variation of fault kinematic data. Abbreviations: SS = strike-slip faulting, TF = thrusting/inverse faulting, NF = normal faulting.

Fig. 6.8 b shows the variation of R (stress ratio) along strike of the study area. R gives insights into the geometry of the strain ellipsoid (flattening/oblate, plane strain, constriction/prolate): R varies very little around a mean value of 0.49 (± 0.07 at a 1σ level) throughout the area. Only one thrust tensor in the north of the study area (PAN082) consistent with flattening ($R = 0.17$), and a normal fault tensor (EBA042) and a strike-slip tensor (PAN069) both consistent with constriction ($R = 0.64$ and $R = 0.69$, respectively) deviate significantly from this pattern. The constancy of R -values around 0.5 indicates that the deformation is plane strain simple shear at a local scale.

Fig. 6.8 c shows the variation in strike of the maximum horizontal stress S_{Hmax} interpreted as the direction of local finite shortening in the horizontal plane. In the case of strike-slip and contractional deformation, S_{Hmax} corresponds to the azimuth of P-axes. In the case of extensional deformation, S_{Hmax} is parallel to the azimuth of the B-axes. Local shortening axes associated with strike-slip deformation vary throughout the study area between NE and ESE due to kinematic partitioning as discussed above. There is no change of this pattern along strike suggesting that this variation is a feature of regional character. Local shortening axes related to inverse faulting in the north of the study area fall within the same range of orientations suggesting that they are kinematically linked to the dominant strike-slip system. Local shortening axes related to normal faults in the northern part of the study area, however, vary from N to S suggesting that along-arc extension as well as normal-to-the-arc extension modify the general strike-slip pattern here.

To summarize, the intra-arc neotectonic (Pliocene to recent) local deformation field between 39° and 42° S is relatively uniform and indicates bulk plane strain strike-slip tectonics characterized by a bimodal distribution of directions of horizontal shortening due to kinematic partitioning into the SC-like LOFZ system. In the northern part of the study area, the deformation field is locally modified by local tectonic regimes including normal and inverse faulting. This modification most likely reflects the influence of the horsetail structure at the northern end of the LOFZ as proposed by Potent and Reuther (2001).